PAPER

Rotating squares auxetic metamaterials with improved strain tolerance

View the article online for updates and enhancements.

DISCOVER how sustainability intersects with electrochemistry & solid state science research

Rotating squares auxetic metamaterials with improved strain tolerance

A Sorrentino , D Castagnetti , L Mizzi and A Spaggiari

Dipartimento di Scienze e Metodi dell'Ingegneria, Università di Modena and Reggio Emilia, Via G. Amendola 2, 42122 Reggio Emilia, Italia

E-mail: andrea.sorrentino@unimore.it, davide.castagnetti@unimore.it, luke.mizzi@unimore.it and andrea.spaggiari@unimore.it

Abstract

Rotating squares auxetic metamaterials have the peculiar feature of a negative Poisson's ratio. This work proposes and examines how an innovative variable arcs fillet solution, at the interconnection regions between the rotating units, improves the structural response of a titanium alloy-based rotating squares metamaterial. Through a 2D finite element (FE) model of the auxetic structure, we investigated and optimized two fillet configurations: first, a double circular arcs profile; second, a combined elliptical and circular arc fillet. According to the FE results, the optimal configuration of the combined elliptical and circular arc fillet allows an overall 3% elastic strain of the metamaterial, with a Poisson's ratio (PR) equal to ca. -1. In order to assess the deformation behavior of the proposed metamaterial, we performed a tensile test on a prototype of the optimal solution, 3D printed in Onyx material. The experimental displacement field of the specimen, measured through digital image correlation, exhibited excellent agreement with the FE predictions, with a PR equal to ca. -1 up to a 3% overall strain.

(Some figures may appear in colour only in the online journal)

1. Introduction

Negative Poisson's ratio (NPR) materials, also known as auxetics [1–7], exhibit the counter-intuitive property of expanding laterally upon the application of a uniaxial tensile strain and other advanced functionalities [8] including higher shear stiffness [9], indentation resistance [10, 11], energy dissipation [12, 13], fracture toughness [14] and synclastic behavior [15]. These systems fall under a class of structures with 'negative' properties which include also metamaterials possessing negative thermal expansion [16–18] and stiffness [19]. Auxetic structures have been widely studied throughout the years [20–24] and have been proposed for use in a number of applications, particularly in the biomedical [25, 26], personal protection [27] and electronics sectors [28, 29]. The unusual mechanical behavior of these materials originates primarily from their geometry, which makes auxeticity scale-independent. Based on deformation mechanisms and their geometry, three main classes of auxetic structures can be identified: re-entrant structures [30, 31], chiral structures [3, 32,

33] and rotating rigid unit structures [34–37]. In particular, the rotating squares system, first proposed by Grima *et al* [38], was extensively studied in recent years [39]. The NPR mechanism proposed by Grima [38], consists of rotating squares connected through simple hinges at the vertices, that is completely described by the following two geometrical parameters: the length of the unit, l, and the angle, θ (see figure 1). This mechanism ensures that when the system is loaded, the squares rotate, either contracting or expanding the overall system depending on whether a compressive or tensile load is applied. As a result of this mode of deformation, the system exhibits in-plane isotropy with a Poisson's ratio of -1. Rotating squares systems have also been designed and manufactured using single-material systems, where the idealized 'joints' in the original model [38], were replaced by fused interconnections between the square units. The stiffness and the auxeticity of these systems depend strongly on the type of connection between the rotating squares.

The interconnection regions of these systems are subjected to large stress concentrations during loading, which makes
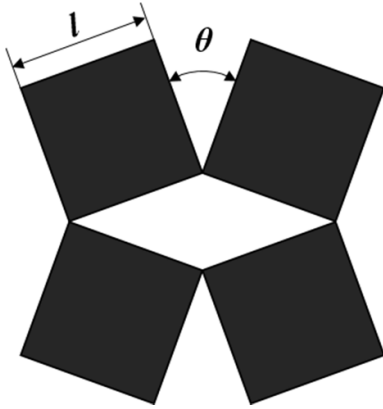
Figure 1. Representative unit cell (RUC) of rotating squares model.

them unsuitable for large strain deformations in the case of systems made from materials with an inherently low strain tolerance. Stress concentrations at the interconnection regions for rotating units auxetic systems also remarkably limit the fatigue life for these types of structures [40]. As reported in the work of Tang *et al* [41], which focused on polymeric materials fabricated via direct-laser cutting, the amount of permissible strain on the rotating squares system is related to the peak elastic stress in the interconnection regions. Thus, to improve the global strain tolerance of these systems some form of geometric optimization is required in these regions [42]. This is particularly pertinent in the case of metal-based auxetic systems, where the material reaches the plastic region at very low strains. The majority of works found in literature concerning the design of titanium alloy-based auxetic metamaterials for use in biomedical devices such as implants and scaffolds have focused mainly on the design, fabrication and characterization of ligament-based structures [43] while there have also been other studies on re-entrant [44], chiral [45] and triangle-square-wheels metallic auxetic systems [46]. On the other hand, there are very few studies centered on the design of metal-based rotating unit systems. As highlighted by Kolken *et al* [8], simple design and fabrication solutions for the rotating structures manufactured via additive manufacturing have yet to be fully investigated, especially 3D printing metallic structures made of titanium alloy. The present work focused on the design, optimization and validation of a metallic rotating squares system with NPR, with particular attention to the shape of the interconnecting regions of the rotating units. The main aim of this work is to reduce the maximum von Mises stress, while keeping the PR of the structure at ca. −1 and maximizing the effective Young's modulus. Inspired by the solution of variable notch radius proposed by Sorrentino *et al* [47] and Pedersen *et al* [48], we propose the use of a variable arcs fillet at the interconnection regions of the rotating squares. Specifically, we implemented a 2D finite element (FE) model of the structure and the analysis involved two steps: in the first step, we optimized a double circular arcs profile at the interconnection regions, while in the second step, the investigation focused on a combined elliptical and circular arcs shape at the interconnection regions. According to the numerical results, a combined elliptical and circular arcs fillet allows the system

to reach a global elastic strain equal to 3%, whilst maintaining a PR equal to ca. −1. In particular, we highlight that a global elastic strain of 3% is significantly higher than the allowable elastic strain of the titanium alloy [49]. To further investigate this optimized solution, we built a sample in Onyx through 3D printing and performed a tensile test by measuring the displacement field of the specimen through digital image correlation (DIC). The experimental results confirmed that the PR of the specimen was equal to ca.−1 for strains up to 3%, in accordance with the FE predictions. Thanks to the peculiar fillet geometry, the proposed solution significantly reduces stress concentrations at the interconnection regions, combined with an easy manufacturing compared to others fillet solutions from the literature [41, 42]. This fillet geometry can be applied both in case of vibration dampening problems and for morphing airfoil applications of aerospace wings [50, 51].

2. The variable arcs fillet geometries

The present work investigated the 2D rotating squares mechanism shown in figure 1. In order to avoid the structural limits of the region that connects the squares, the focus is on identifying the optimal shape of the interconnecting regions of the rotating units. Two solutions are investigated in this work: first, a double circular arc fillet (figure 2(a)) and second, a fillet that combines an elliptical arc and a circular arc (figure 3(a)). For both solutions, there are two geometrical parameters that define the RUC of the rotating square model (figures 2(a) and 3(a)): the length of the square lattice, L, and the angle between the rigid units, θ:

$$L = 2L_0 \tag{1}$$

$$\theta = 180° - \gamma \tag{2}$$

where L_0 is the side length of a quarter of the RUC (i.e. a rotating square), and γ is the supplementary (internal) angle of the structure. For each solution proposed here, figures 2(b) and 3(b) show in detail the geometric configuration of a rotating square, corresponding to a quarter of the RUC: D represents the side length of the rigid square, while $l_1 = D/2$ is the side length of the simulated structure that when periodically repeated gives the unit square. l_3 and l_2, identify the start points of the fillet. Figures 2(c) and 3(c), show a close-up view of the two variable arcs fillet geometries proposed in this work that characterize each simulated structure, where s represents the width of the ligament at the interconnection region. Specifically, the double arcs shape solution in figure 2(c) connects the ligament to the square with a double circular arcs fillet (radius R_1 and R_2). To build this geometry, tangency conditions are imposed in four points: between the smaller arc, R_2, and the perimeter of the simulated structure (i.e. points '*a*' and '*b*' in figure 2(c)), and between the two arcs of the fillet (i.e. points '*c*' and '*d*' in figure 2(c)). Consequently, the dimensions l_2 and l_3 (figure 2(b)), depend on the side length, l_1, of the simulated structure and from the radii R_1 and R_2. Similarly,
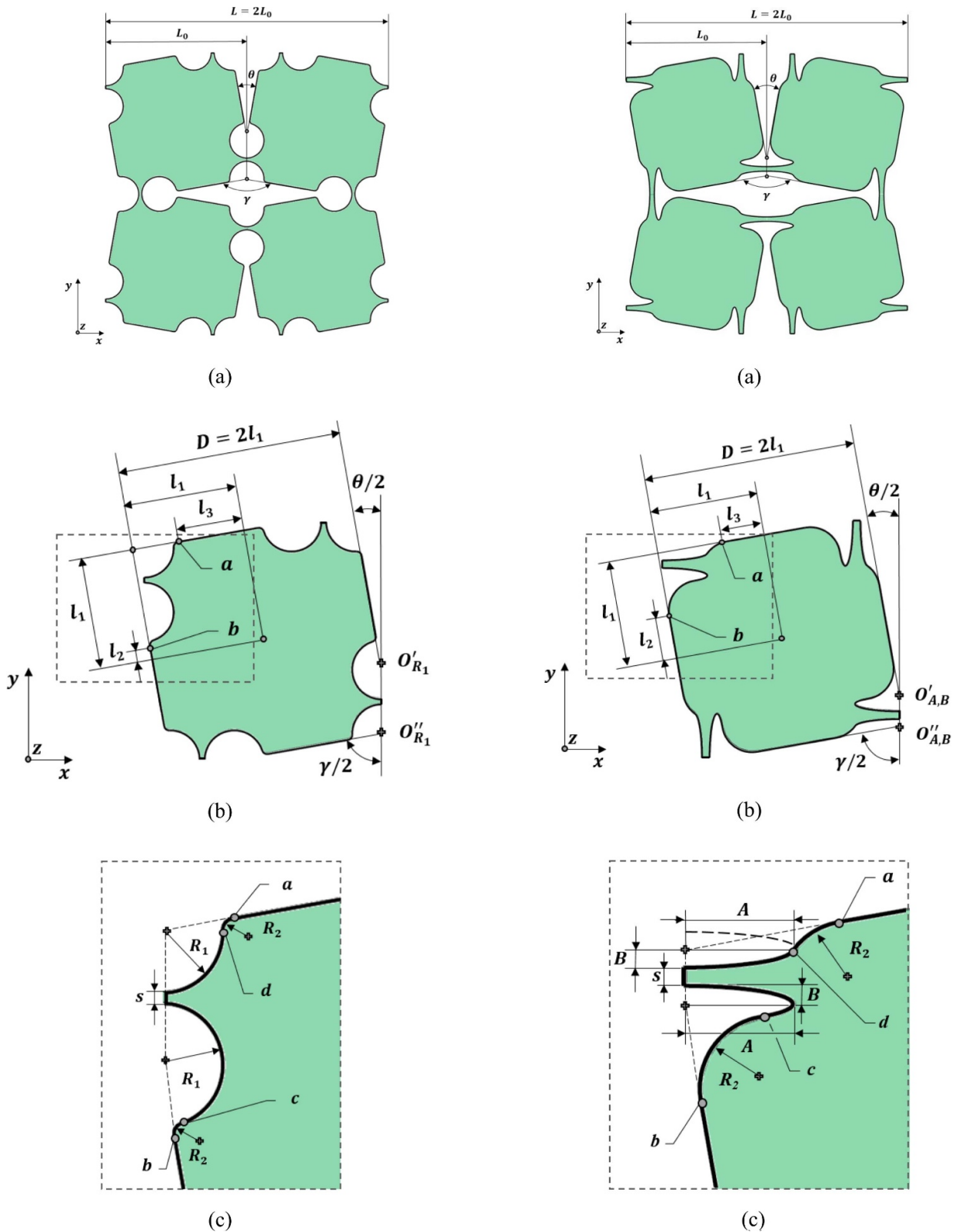
Figure 2. RUC of the rotating squares system with double circular arcs profile at the interconnection regions (a), unit cell (b), detailed fillet geometry at the interconnection regions (c).

Figure 3. RUC of the rotating squares system with a combined elliptical and circular fillet profile at the interconnection regions, unit cell (b), detailed fillet geometry at the interconnection regions (c).

the solution in figure 3(c), connects the ligament to the simulated structure through an elliptical arc combined with a circular arc fillet: *A* and *B* in figure 3(c) are the two semi-axes

of the elliptical arc, while R_2 is the radius of the circular arc. In this case, the tangency conditions applied are: between the circular arc, R_2, and the perimeter of the simulated structure

(a)

(b)
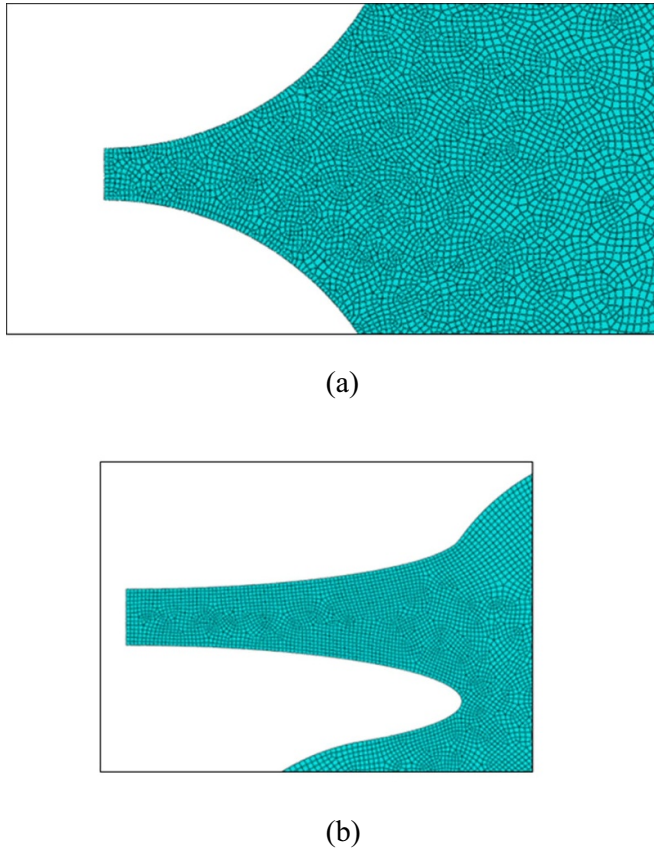
Figure 4. Details on the FE model mesh with double circular arc fillet (a) and for the combined elliptical and circular fillet solution at the interconnection regions (b).

(i.e. points '*a*' and '*b*' in figure 3(c)), and between the elliptical arc and the circular arc (i.e. points '*c*' and '*d*' in figure 3(c)). As for the previous case, the dimensions, l_2 and l_3 (figure 3(b)) are then expressed as a function of the side length, l_1, of the simulated structure minus the dimensions of the elliptical and circular arc.

3. The FE model analysis

In order to investigate the structural response, we implemented a 2D FE model of both the structures proposed in the previous section, using the commercial FE software Abaqus 6.20 [52]. Taking advantage of the highly symmetric nature of the rotating square system, the system was simulated as a quarter of the RUC [53] (see figures 2(b) and 3(b)). A fixed width for the thinnest section of the interconnecting region was used for all simulations, $s = 1$ mm. The mesh consists of 2D plane-stress elements, with quadratic formulation (CPS8 [52]). Following a mesh convergence analysis, the average element side length in the interconnecting regions was set equal to 0.05 mm (with about 20 elements in the thinnest part of the connection), while an average side length equal to 0.1 mm was used for the remaining part of the model. Figure 4 shows a detail of the mesh refinement on the ligament region for the double circular arc solution (figure 4(a)), and for the combined elliptical and circular fillet solution (figure 4(b)).

Since we focused on the maximum equivalent elastic stress in the auxetic system, the material used was that of an isotropic elastic titanium alloy material (Ti6Al4V) produced by selective laser melting (SLM) [49]. Specifically, the model applies a Young's modulus, E, equal to 110 000 MPa, and a Poisson's ratio, ν, equal to 0.3; and considers a maximum allowable stress (i.e. yield stress), R_s, equal to 1013 MPa [49]. Focusing on the unit square of the RUC with double circular arcs profile at the interconnection regions, figure 5 shows the boundary conditions and the applied load for the double circular arc solution. The rotating unit cell is simply supported in the nodes on the bottom edge (s_h^b in figure 5) and on the left edge (s_v^l in figure 5) of the cell. In order to implement the periodic symmetry of the unit square of the RUC, the nodes on the right edge (s_v^r in figure 5) were coupled for equal displacement in the *x*-directions [53, 54]. The system was loaded through the application of a displacement, u_y, on the upper edge nodes (s_h^t in figure 5). This displacement was proportional to the side length of the unit square, according to the following relationship:

$$u_y = L_0\,\varepsilon_y \tag{3}$$

where $\varepsilon_y = 3\%$ is the global strain applied on the unit square in the *y*-direction. The same loading method was also applied for the combined elliptical and circular fillet systems.

Thanks to the inherent geometric symmetry of the structure, these boundary conditions are identical the PBCs and has been validated by comparison with the simulation of an entire RUC under PBCs using the Abaqus plug-in by Omairey *et al* [55].

To evaluate the mechanical response of the system, we performed a nonlinear static analysis [53], and calculated the effective Poisson's ratio, v_{yx}^*, and the effective Young's Modulus, E_y^*, of the auxetic structure, assuming unit thickness, using:

$$v_{yx}^* = -\frac{u_x}{u_y} \tag{4}$$

and

$$E_y^* = \frac{\sum \mathrm{RF}_{y,i}}{L_0\varepsilon_y} \tag{5}$$

where u_x is the horizontal displacement of the nodes on the right vertical ligament (s_v^r in figure 5) and $\mathrm{RF}_{y,i}$ is the reaction force in the *y*-direction of the *i*th node in the loaded edge ligament (s_h^t in figure 5). In addition, the maximum von Mises stress in the system, σ_{vm}^{max}, was also measured.

3.1. The double circular arcs shape optimization

The first analysis focused on the design and optimization of a rotating squares auxetic system with a double circular arcs profile at the interconnection regions (figure 2(a)). Since the structure under investigation has a Poisson's ratio lower than −0.95, due to its intrinsic configuration, the optimization problem aimed to: (a) minimize the maximum von Mises stress, σ_{vm}^{max}, in the structure (usually occurring in the interconnection regions); (b) maximize the effective Young's Modulus,
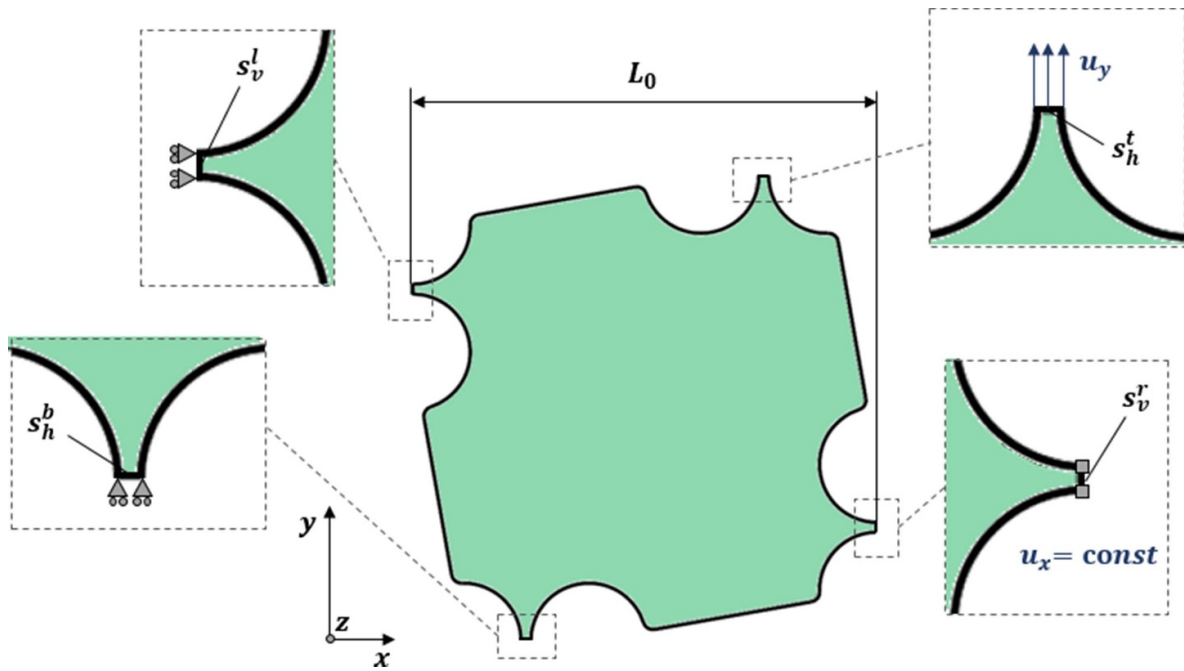
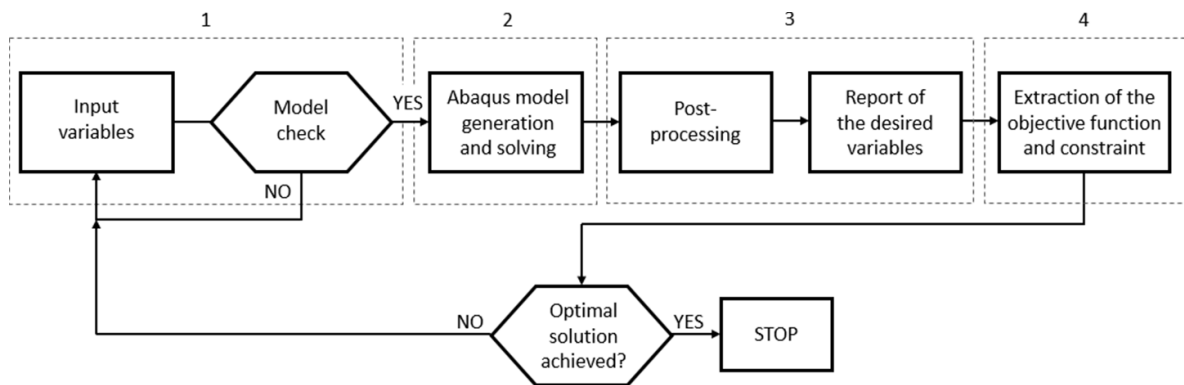**Figure 5.** 2D FE model of the rotating squares system with prescribed periodic boundary conditions (PBCs).

Figure 6. Optimization workflow.

E_y^*, of the system, while maintaining an effective Poisson's ratio, v_{yx}^* lower than -0.95. Thus, the optimization problem can be defined as:

$$\min \frac{\sigma_{vm}^{max}}{E_y^*} \tag{6}$$

$$s.t.\, v_{yx}^* < -0.95 \tag{7}$$

where equations (6) and (7) represent the objective function and the constraint of the optimization problem, respectively. In order to find the optimal radius of the two arcs and the corresponding dimensions of the rotating unit, we implemented an ad-hoc, automated shape optimization procedure that combines a genetic algorithm with a parametric, 2D FE model of the auxetic mechanism. Assuming a constant unit width for the ligament at interconnection regions, ($s = 1\,mm$), the shape optimization problem involves four design variables: the

angle θ, the two radii, R_1 and R_2, and the length, l_2, of the simulated cell (figure 2(b)). Considering the overall dimensions of the structure and the fixed unit width, s, of the ligament in the interconnection region, the constraints on the fillet radii were $1\,mm < R_1 < 10\,mm$ and $1\,mm < R_2 < 10\,mm$, respectively. The constraints on the length of the simulated cell and on the angle of the rotating unit cell were $1\,mm < l_2 < 10\,mm$ and $20° < \theta < 160°$, respectively. It is easy to observe that the length of the rotating square, $2l_1$, and the length of the RUC quarter of the system, L_0 (see figure 2), are a function of the design variable l_2. In addition, the value of the second dimension of the rotating unit, l_3, can be simply retrieved from the length, l_1, of the rotating square and of the two angles, θ and γ (figure 2). The shape optimization problem was implemented through the commercial optimization software VisualDOC 8.0 [56], which managed the nonlinear stress analysis through the FE software Abaqus 6.20: in order to set-up a completely automatic optimization procedure, the FE model was parametric

Table 1. Specification of the optimization problem for the case of double circular arc fillet.

Geometry fillet	Design variables	Objective function	Constraints
Double circular arc	$20° < \theta < 160°$ $1\,\text{mm} < l_2 < 10\,\text{mm}$ $1\,\text{mm} < R_1 < 10\,\text{mm}$ $1\,\text{mm} < R_2 < 10\,\text{mm}$	$\min \frac{\sigma_{\text{vm}}^{\max}}{E_y^*}$	$\varepsilon_y = 3\%$ $l_3 \geq s$ $v_{yx}^* < -0.95$

and described using the Python language scripts [57]. Figure 6 shows the design workflow of the shape optimization problem, which is similar to the optimization workflow described in the work of Sorrentino *et al* [47].

The shape optimization problem involves the following four steps. First, the optimization software assigns trial values to the four design variables and checks the feasibility of the rotating squares model, by verifying the following constraint:

$$l_3 \geq s \tag{8}$$

where $s = 1\,\text{mm}$, represents the minimum length in the auxetic mechanism. Second, the optimization software sends the design variables (θ, R_1, R_2 and l_2) to the Abaqus software, where the input Python language script automatically generates the model and solves the analysis. Third, an input Python script reads the result file from the FE model and stores in a report file the following three variables: first, the displacement of the unfixed vertical edge of the system, u_x, second, the reaction forces in *y*-direction on all the nodes in the loaded edge ligament, RF_y, and third, the maximum von Mises stress on the system, $\sigma_{\text{vm}}^{\max}$ (see section 3). Fourth, the optimization software receives back this report file, extracts the objective function and the constraint defined as in equations (6) and (7), and compares these values with the ones from the previous iteration, where, E_y^* and v_{yx}^*, were calculated as shown in equations (4) and (5). The optimization process described above iterates until the optimal solution is achieved. Specifically, we used a penalty-constrained particle swarm optimization algorithm [58] to manage the optimization problem, with a number of particles, n, equal to 30. Thus, the optimization problem can be defined as shown in table 1.

3.2. The combined elliptical and circular arcs shape optimization

The second step of the work investigates the deformation behavior of a rotating squares auxetic metamaterial with a double arc fillet at the interconnection regions by replacing the first circular arc (R_1 in figure 2) with an elliptical shape solution where, A and B, represents the major and minor semi-axes of the elliptical arc, respectively (figure 3). As for the case of double circular arc fillet solution, the analysis aims to: first, minimize the maximum von Mises stress in the structure, $\sigma_{\text{vm}}^{\max}$; second, maximize the effective Young's modulus, E_y^*, of the system, while keeping an effective Poisson's ratio, v_{yx}^*, ca. -1. Thus, we fixed the width of the ligament at interconnection

regions, s, equal to $1\,\text{mm}$ (see section 2). The global strain and the stiffness of the auxetic mechanism are affected by the side length of the rotating unit, D, by the angle between the squares, θ, and by the stiffness at the interconnection regions, which depends on the semi-axes of the elliptical arc, A and B (figure 3). As shown in the works of Grima *et al* [38, 59], for a Poisson's ratio, v_{yx}^*, equal to -1, the effective Young's modulus of the system, E_y^*, increases by reducing the simulated cell length, l_1, for fixed values of θ (see figure 3). Specifically, if we choose small values of l_1 and θ, a further increase of the stiffness of the system can be obtained by reducing the dimensions of the two semi-axes of the elliptical shape fillet, A and B [47, 48]. Thus, the simulated cell length, l_1, the semi-axes of the elliptical arc, B, and the angle θ, were set equal to [38]:

$$l_1 = 14\,\text{mm}$$
$$B = s = 1\,\text{mm}$$
$$\theta = 20° \tag{9}$$

Given the above assumptions, the variables of the optimization problem were two: first, the major semi-axis of the elliptical shape, A and second, the radius of the circular arc, R_2 (figure 3). Specifically, the value of l_1 equal to 14 mm, allows to vary the major semi-axes of the elliptical arc, A, up to relatively large values while keeping the relevant auxetic response of the rotating mechanism [59]. Given the complexity of the geometry, the optimization was split in two steps: first, we fixed R_2 to a 1 mm value and found the A semi-axis that maximizes the stiffness of the auxetic material and provides an effective Poisson's ratio equal to -1, for a global elastic strain up to 3%. Specifically, we investigated four levels of the semi-axis A, from 12 mm to 6 mm. Second, from the optimal solution found in the first step, we examined the effect on the stress concentration at the interconnection regions of the radius of the circular arc, R_2. For this step, the four levels of the radius fillet investigated vary from 1 mm to 4 mm. The nonlinear static analysis performed was the same described in section 3. For each configuration evaluated in both steps, the optimization procedure calculated the effective Poisson's ratio, v_{yx}^*, the effective Young's modulus of the system, E_y^*, (see equations (4) and (5)), and the maximum von Mises stress, $\sigma_{\text{vm}}^{\max}$. Table 2 summarize the optimization problem defined above.

4. Numerical optimization results

Table 3 reports the optimal dimensions of the rotating units and of the ligaments at the interconnection regions for the two fillet geometries investigated through the FE analysis in section 3, with the first row showing the double circular arcs profile (see figure 2) and the second row, the combined elliptical and circular fillet solution (see figure 3), for a fixed width of the ligament, $s = 1\,\text{mm}$.

With reference to the combined elliptical and circular shape fillet (step 1 of the optimization procedure in section 3.2), the diagram in figure 7 shows the value of normalized peak von

Table 2. Specification of the optimization problem for the case of combined elliptical and circular arcs solution.

Geometry fillet	Step	Design variables	Objective function	Constraints
Combined elliptical and circular arcs	1	$6\,\text{mm} < A < 12\,\text{mm}$ $R_2 = 1\,\text{mm}$	$\min \dfrac{\sigma_{\text{vm}}^{\max}}{E_y^*}$	$\varepsilon_y = 3\%$ $l_1 = 14\,\text{mm}$ $B = 1\,\text{mm}$ $\theta = 20°$ $v_{yx}^* < -0.95$
	2	$A = 6\,\text{mm}$ $1\,\text{mm} < R_2 < 4\,\text{mm}$		

Table 3. Optimal dimensions of the unit cell and of the two fillet geometries investigated.

Geometry fillet	l_1 (mm)	L_0 (mm)	θ (mm)	R_1 (mm)	R_2 (mm)	A (mm)	B (mm)
Double circular arc	22.7	48.2	20	6	1	/	/
Combined elliptical and circular fillet	14	31.6	20	/	4	6	1
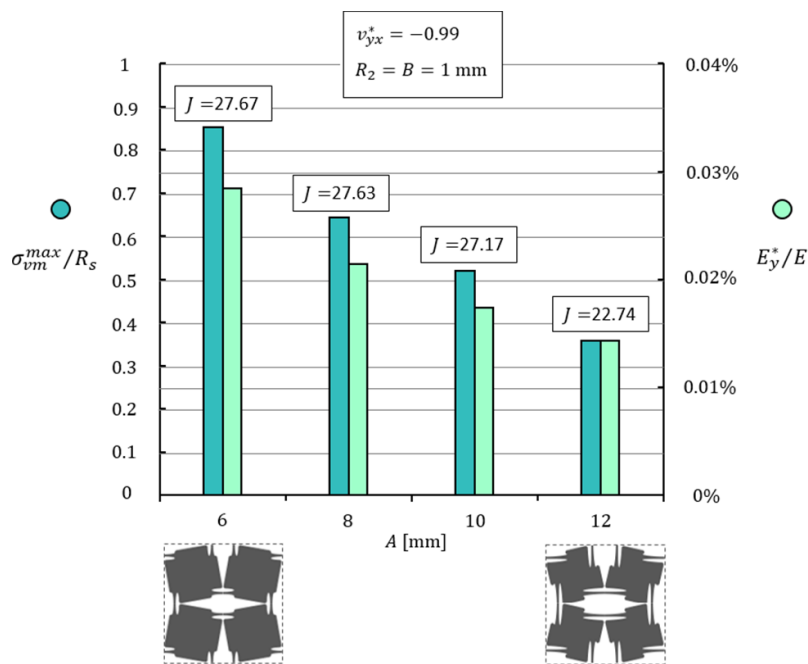
Figure 7. Normalized peak von Mises stress, $\sigma_{\text{vm}}^{\max}/R_s$, and normalized effective Young's Modulus, E_y^*/E, of the auxetic structure with the corresponding value of the objective function, J (i.e. $\sigma_{\text{vm}}^{\max}/E_y^*$ in table 2); for different levels of the major semi-axes of the elliptical arc, A, for the combined elliptical and circular shape fillet.

Mises stress, $\sigma_{\text{vm}}^{\max}/R_s$, and the normalized effective Young's modulus of the system, E_y^*/E, as a function of the variation of the major semi-axis of the elliptical arc, A, for a fixed $R_2 = 1\,\text{mm}$. Similarly, the diagram in figure 8 relates the normalized peak von Mises stress and the normalized effective Young's modulus of the system to the radius of the circular arc, R_2, for fixed $A = 6\,\text{mm}$ (step 2 of the optimization procedure in section 3.2). Specifically, the auxetic geometries in figures 7 and 8 show an effective PR, v_{yx}^*, very close to -1, which is due to its intrinsic configuration.

Additionally, figures 7 and 8 report the value of the optimization function (i.e. $\sigma_{\text{vm}}^{\max}/R_s$ in table 2), defined as J.

Table 4 compares the mechanical properties and the maximum von Mises stress, $\sigma_{\text{vm}}^{\max}$, for a global strain, $\varepsilon_y = 3\%$, of the optimal metamaterial configurations identified through the FE analysis: E_y^* and v_{yx}^* were calculated using equations (4)

Table 4. Mechanical properties of the two fillet geometries investigated.

Geometry fillet	v_{yx}^* (adm)	E_y^* (MPa)	$\sigma_{\text{vm}}^{\max}$ (MPa)
Double circular arc	-0.99	42.70	$> R_s$
Combined elliptical and circular fillet	-0.99	31.22	864

and (5), and $R_s = 1013\,\text{MPa}$ is the yield stress of the titanium alloy [49].

Figure 9 shows the von Mises stress contour acting on a unit cell, with a close-up view of the ligament: figure 9(a) refers to the optimal double circular arcs, while figure 9(b) to the combined elliptical and circular shape fillet.
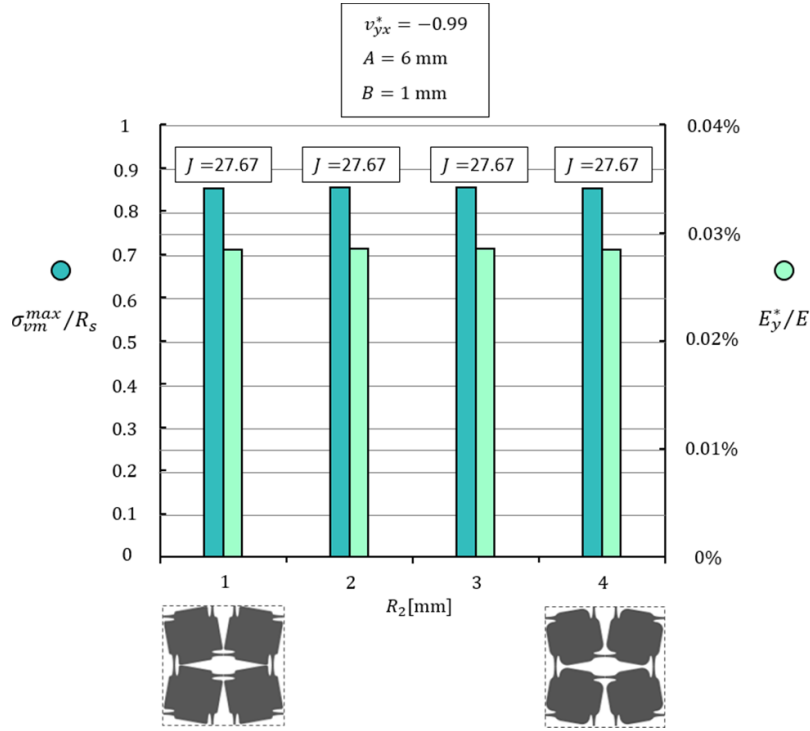
Figure 8. Normalized peak von Mises stress, σ_{vm}^{max}/R_s, and normalized effective Young's Modulus, E_y^*/E, with the corresponding value of the objective function, J (i.e. σ_{vm}^{max}/E_y^* in table 2); for different levels of the circular arc, R_2, for the combined elliptical and circular shape fillet with fixed A.

5. Experimental validation

The experimental validation focused on the combined elliptical and circular arc shape solution (figure 3), since, according to the analysis in sections 3 and 4, it provides the best structural response.

5.1. Prototype development

Using the optimal dimensions of the RUC reported in the second row in table 3, we built a prototype composed by a 3×3 RUC system, giving and overall 190 mm × 190 mm side length. In order to have a plane response, the structure thickness in the out-of-plane direction was equal to 10 mm. Since the deformation behavior of the structure is independent from its material, we manufactured the prototype using a fused filament fabrication Markforged® 3D printing machine in Onyx material (figure 10(a)): the specimen included a top and bottom plate to ensure an equal deformation all over the width of the structure.

5.2. Test procedure

The prototype was uniaxially stretched using a Galdabini SUN 500 electromechanical testing machine with a 5 kN load-cell, controlled by a PC equipped with the proprietary software Graphwork [60]. The quasi-static tensile test applied a 5.7 mm stroke to the sample at a rate of 1 mm min^{-1}, which corresponds to an overall global strain of the sample equal to 3%. In order to evaluate the Poisson's ratio of the structure, we measured the displacement field of the central RUC of the sample (figure 10(b)) using a Dantec Dynamics Digital Image Correlation system and analyzed the response through the ISTRA 4D software.

5.3. Experimental results

Figure 11 compares the initial configuration (figure 11(a)) with the final configuration (figure 11(b)) of the central RUC of the sample (figure 10) where, ΔL_y and ΔL_x, represent the axial and the transverse elongation of the RUC, respectively, and where, L, is the original side length of the central square lattice.

By tracking the displacement components (axial and transverse direction) of the eight marker points on the RUC, one on each end of the eight ligaments of the central RUC (green dots in figure 10(b)), the DIC calculated the Poisson's ratio of the sample. Thus, the average strains in y and x directions are computed as follow [61]:

$$\bar{\varepsilon}_y = \frac{1}{2}\left[\frac{\left(Y_1^i - Y_3^i\right) - \left(Y_1^0 - Y_3^0\right)}{\left(Y_1^0 - Y_3^0\right)} + \frac{\left(Y_2^i - Y_4^i\right) - \left(Y_2^0 - Y_4^0\right)}{\left(Y_2^0 - Y_4^0\right)} \right] \tag{10}$$

and

$$\bar{\varepsilon}_x = \frac{1}{2}\left[\frac{\left(X_5^i - X_7^i\right) - \left(X_5^0 - X_7^0\right)}{\left(X_5^0 - X_7^0\right)} + \frac{\left(X_6^i - X_8^i\right) - \left(X_6^0 - X_8^0\right)}{\left(X_6^0 - X_8^0\right)} \right] \tag{11}$$

(a)

(b)
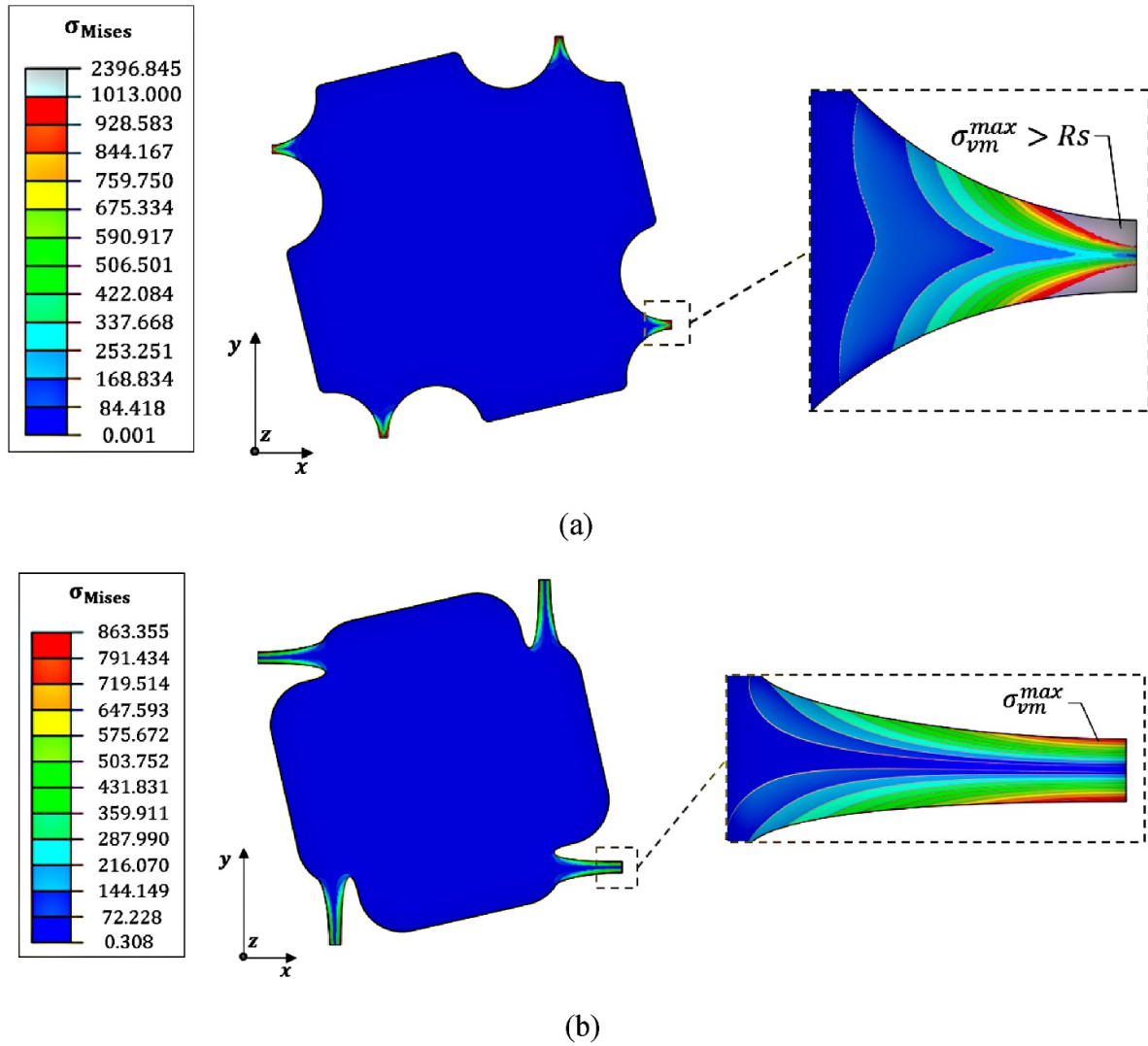
Figure 9. Von Mises stress contour for the case of double circular arcs profile (a) and for the combined elliptical and circular shape solutions at the at the interconnection regions (b).

where Y_j^0 and X_j^0 represent the *y* and *x*-coordinates of the points in the initial configuration (figure 11(a)), and Y_j^i and X_j^i the corresponding *y* and *x*-coordinates of the same points in the final configuration (figure 11(b)). Then, we calculated the experimental Poisson's ratio, v_{yx}^*, namely:

$$v_{yx}^* = -\frac{\bar{\varepsilon}_x}{\bar{\varepsilon}_y} \tag{12}$$

In this regard, table 5 compares the numerical and experimental effective Poisson's ratio for the optimal rotating unit system with the combined elliptical and circular fillet solution at the interconnection regions.

6. Discussion

The optimal dimensions of the rotating unit with a combined elliptical and circular arcs shape fillet are significantly smaller than the ones of the double circular arc shape solution, with a

Table 5. Comparison between the numerical and experimental PR of the optimal auxetic system found with a combined elliptical and circular fillet shape.

Geometry fillet	v_{yx}^*(adm)	
	FE	DIC
Combined elliptical and circular fillet	−0.99	−1.01

side length of a quarter of the RUC, L_0, equal to 31.6 mm and with a length of the simulated structure, l_1, equal to 14 mm (see table 3). This gives a RUC which is 34% smaller than the one with the double circular arc solution, that allow its application in a large number of engineering applications. For both the solutions investigated, the optimization procedure suggests an angle, θ, between the rotating units, equal to 20°, corresponding to the lower bound of the domain defined in the optimization analysis (see sections 3.1 and 3.2). The small value of θ found in the first optimization analysis (i.e. for the case of double circular arcs), supports the assumptions made in the
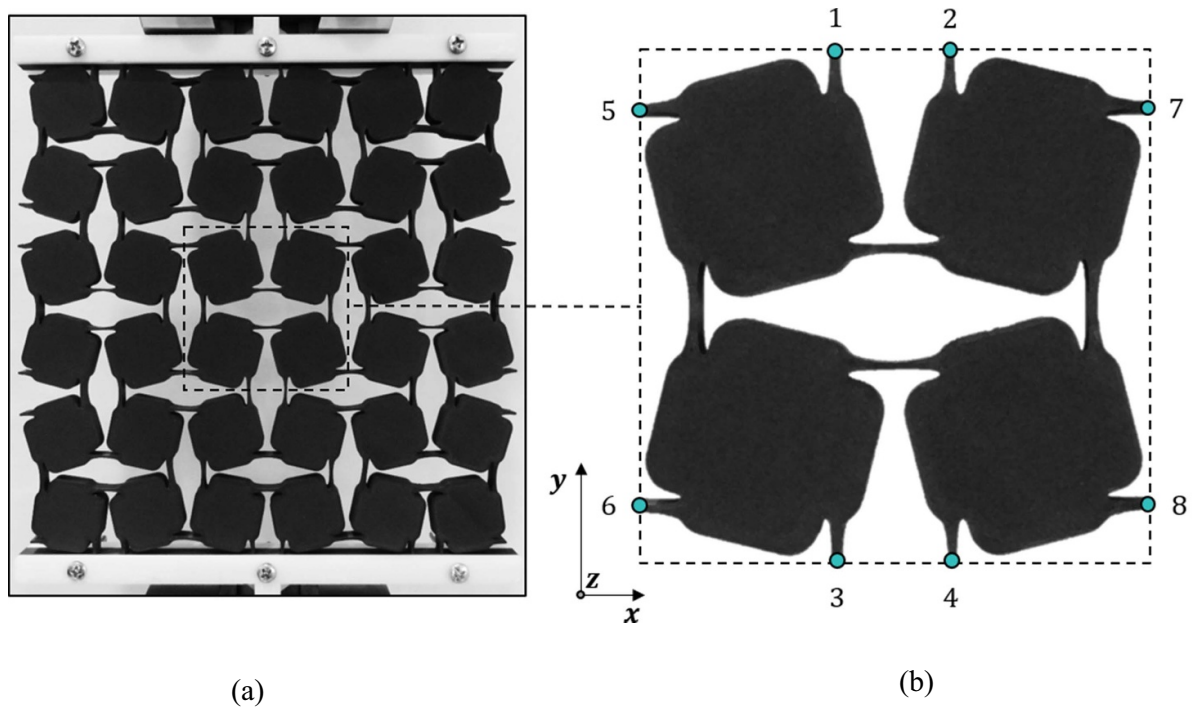
Figure 10. Experimental prototype tested (a) and central RUC with the points used for tracking the displacements (b).
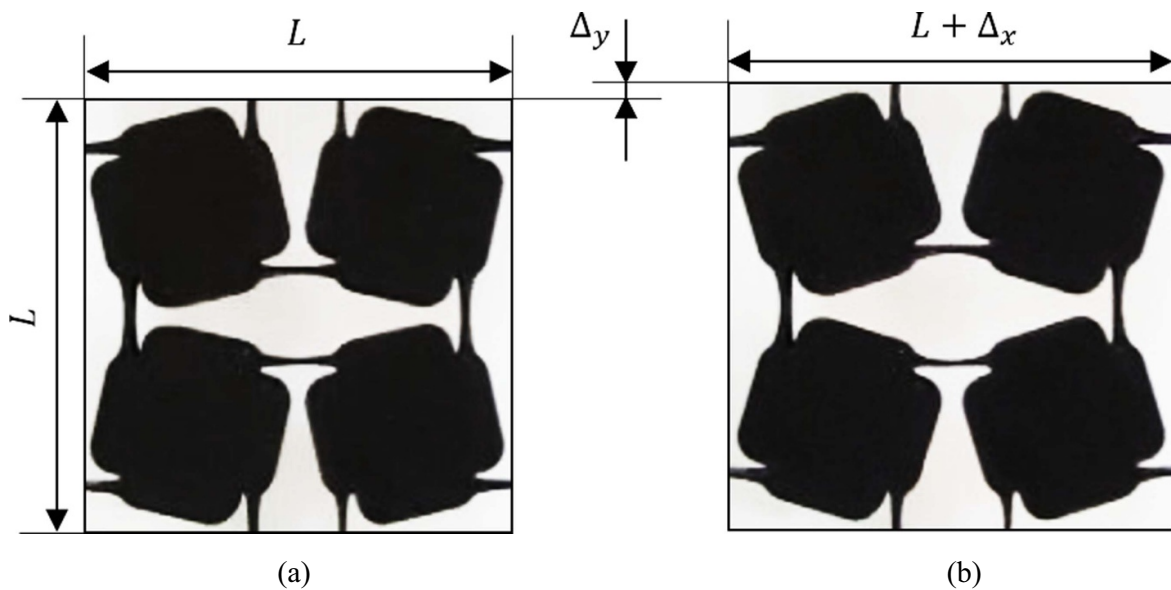
Figure 11. Initial (a) and final (b) configuration of the central RUC.

second optimization step (i.e. for the case of combined double arcs solution), in accordance with the theoretical models from the works of Grima *et al* [59].

Three observation can be made from table 4. First, the effective Poisson's ratio, v_{yx}^*, of the two optimized auxetic structures proposed is very close to −1, which corresponds to the maximum PR achieved from the theoretical predictions [38, 59]. In addition, in order to increase the PR of the structure, we need to remove material from the semi-rigid part of the squares [62], and at same time, consistently reduce

the dimensions of the rotating units: this leads to obtain a structure similar to a chiral systems. As shown in table 2, the auxetic behavior of the system is not affected by the type of connections between the rotating squares for both the shape fillet solutions investigated. Second, table 4 highlights that the effective Young's modulus, E_y^*, differs between the two geometries: 42.70 MPa for the double circular arc shape solution, and 31.22 MPa for the combined elliptical and circular arcs shape. Three are the geometrical factors that affect the value of E_y^*: first, the side length of a quarter of the RUC, L_0; second, the

angle θ; third, the variable arcs fillet dimensions (see figures 2 and 3). Specifically, for the case of the double circular arc fillet, the value of the L_0 is determined by the values of the two radii of the double circular fillet, R_1 and R_2 (see section 3.1), that cause an increase of the Young's modulus (see table 2). Otherwise, for the case of the combined elliptical and circular arcs solution with a $L_0 = 31.6\,\mathrm{mm}$, the dimensions of the elliptical arc, A and B, cause a sharp reduction of the Young's modulus E_y^* (see table 2). With regard to the angle θ, the FE predictions suggest that the lower this angle, the lower the effective Young's modulus and the peak elastic stress of the structure: this allows to decrease the dimensions of the auxetic configuration. Third, table 4 shows that only in the combined elliptical and circular arcs solution the peak stress is lower (864 MPa) than the elastic limit of the of the titanium alloy ($R_s = 1013\,\mathrm{MPa}$ [49]). Instead, for the case of double circular arc shape solution, the allowable global elastic strain of the structure is nearly equal to 1.26% of its original length, which is less than half of the elastic strain achieved with the combined elliptical and circular solution. As shown in figure 7, the higher the major semi-axes of the elliptical arc, $A = 12\,\mathrm{mm}$, the lower the values of the normalized effective Young's modulus (with $E_y^* = 15.61\,\mathrm{MPa}$), and of the normalized peak von Mises stress, with $\sigma_{\mathrm{vm}}^{\max}$ equal to 355 MPa. On the other hand, by decreasing the value of A up to 6 mm, the value of E_y^* increases up to a value of 31.22 MPa, with a peak of the stress, $\sigma_{\mathrm{vm}}^{\max} = 864\,\mathrm{MPa}$. Figure 8 points out that, for a fixed configuration of the elliptical arc, the radius of the second arc, R_2, does not affect the auxetic response of the system, nor the peak stress: however, this circular fillet has a beneficial effect to avoids sharp corners on the geometry which are difficult to manufacturing, and to reduce the mass of the system. Moreover, for all the auxetic architectures investigated in figures 7 and 8, the value of the objective function, J, equal to $\sigma_{\mathrm{vm}}^{\max}/E_y^*$; is nearly the same. However, the higher the value of the minor semi-axis of the elliptical arc, B, for fixed values of l_1, the higher the values of the effective Young's modulus and of the peak stress, also for the case of $A = 12$ mm. This fact highlights that there are multiple combinations of the geometrical parameters that allow to obtain similar mechanical properties with different geometrical dimensions of the shape fillet. As one may observe, the stress contours in figure 9, highlight a stress concentration in the interconnection regions, which act as compliant joint and allow to obtain the peculiar kinematic response of the proposed auxetic structure. By comparing the initial and final step of the test in figure 11, it clearly appears the auxetic response of the prototype with the optimal configuration proposed in table 3 (combined elliptical and circular arcs). In addition, as reported in table 5, the experimental PR obtained through the DIC analysis was equal to ca. -1 for strains up to 3% of the structure, in accordance with the FE results, and with the theoretical predictions found from the literature [39, 63] for ideal rotating squares metamaterials.

On the whole, the proposed combined elliptical and circular arcs fillet solution for the interconnection regions, allows for a PR -1, grants a noticeable stress reduction with an improved strain tolerance, and can be easily manufactured. This structure also has a relatively higher stiffness in comparison to ligamented auxetic structures, such as chiral and re-entrant honeycomb. Furthermore, it is worth noting that the fillet solution proposed here involves a trade-off between metamaterial stiffness and strain tolerance, i.e. one can improved the Young's modulus of the system at the cost of lowering the maximum allowable deformation. It also evident from figure 10 that the fillet geometry which permits high deformation has design characteristics which are similar to that found in an anti-tetrachiral honeycombs [32]. This means that in order to improve the strain tolerance of the overall system while retaining high stiffness, one must endeavor to produce an interconnection geometry which is partially a ligament and a 'joint' at the same time. Finally, the same combined elliptical and circular fillet shape solution can also be applied both to different planar rotating (semi-)rigid structures, such as rectangles, rhombi and triangles or to 3D rotating units with cubes or prismatic units [63–65]. This finding potentially opens up a wide range of engineering applications, especially in case of vibration dampening problems and for morphing airfoil applications of aerospace wings [50, 51].

7. Conclusions

The present work investigated the mechanical behavior of a metallic rotating square auxetic metamaterial with a Poisson's ratio of -1. Rotating square auxetic systems are known to have higher stiffness than ligament-based auxetic structures, however they are also characterized by large concentrations of stress at the at the interconnection regions which makes them unsuitable for large strain deformations. The work proposed and optimized an innovative variable arcs fillet shape solution at the interconnection regions of the rotating units: first, a double circular arcs profile, second, a combined elliptical and circular arc fillet shape. In order to evaluate the effective mechanical properties of these structures, we implemented a 2D FE model of the system made of titanium alloy material Ti6Al4V produced by SLM. The numerical results show that only a combined elliptical and circular arc fillet solution allows the system to reach a global elastic strain equal to 3% while maximizing the effective Young's Modulus of the system, with a PR equal to ca. -1. A sample of the optimal solution was also manufactured through 3D printing in Onyx material. The sample was tested with a tensile loading device and DIC measurements were performed. The experimental PR obtained through the DIC measurements was equal to ca. -1, in accordance with the FE results.

ORCID iDs

A Sorrentino ⬚ https://orcid.org/0000-0002-7145-5219
D Castagnetti ⬚ https://orcid.org/0000-0003-3300-5716
L Mizzi ⬚ https://orcid.org/0000-0002-7650-1173
A Spaggiari ⬚ https://orcid.org/0000-0001-8959-2599

References

[1] Evans K E, Nkansah M A, Hutchinson I J and Rogers S C 1991 Molecular network design [7] *Nature* **353** 124

[2] Ren X *et al* 2018 Auxetic metamaterials and structures: a review *Smart Mater. Struct.* **27** 2

[3] Lakes R 1991 Deformation mechanisms in negative Poisson's ratio materials: structural aspects *J. Mater. Sci.* **26** 2287–92

[4] Wojciechowski K W 1989 Two-dimensional isotropic system with a negative poisson ratio *Phys. Lett.* A **137** 60–4

[5] Lakes R 1987 Foam structures with a negative Poisson's ratio *Science* **235** 1038–40

[6] Jopek H and Strek T 2017 Torsion of a two-phased composite bar with helical distribution of constituents *Phys. Status Solidi* b **254** 1–8

[7] Jopek H and Stręk T 2018 Thermoauxetic behavior of composite structures *Materials* **11** 294

[8] Kolken H M A and Zadpoor A A 2017 Auxetic mechanical metamaterials *RSC Adv.* **7** 5111–29

[9] Choi J B and Lakes R S 1992 Non-linear properties of metallic cellular materials with a negative Poisson's ratio *J. Mater. Sci.* **27** 5375–81

[10] Argatov I I, Guinovart-Díaz R and Sabina F J 2012 On local indentation and impact compliance of isotropic auxetic materials from the continuum mechanics viewpoint *Int. J. Eng. Sci.* **54** 42–57

[11] Scarpa F *et al* 2006 Dynamic behavior and damping capacity of auxetic foam pads *Smart Structures and Materials 2006: Damping and Isolation* vol 6169 p 61690T

[12] Evans K E 1991 Auxetic polymers: a new range of materials *Endeavour* **15** 170–4

[13] Hou W, Yang X, Zhang W and Xia Y 2018 Design of energy-dissipating structure with functionally graded auxetic cellular material *Int. J. Crashworthiness* **23** 366–76

[14] Choi J B 1996 Fracture toughness of re-entrant foam materials with a negative Poisson's ratio: experiment and analysis *Int. J. Fract.* **80** 73–83

[15] Scarpa F, Ciffo L G and Yates J R 2004 Dynamic properties of high structural integrity auxetic open cell foam *Smart Mater. Struct.* **13** 49–56

[16] Lakes R 2007 Cellular solids with tunable positive or negative thermal expansion of unbounded magnitude *Appl. Phys. Lett.* **90** 221905

[17] Li D, Ma J, Dong L and Lakes R S 2016 A bi-material structure with Poisson's ratio tunable from positive to negative via temperature control *Mater. Lett.* **181** 285–8

[18] Lim T-C 2019 2D metamaterial with in-plane positive and negative thermal expansion and thermal shearing based on interconnected alternating bimaterials *Mater. Res. Express* **6** 115804

[19] Dudek K K *et al* 2018 Negative and positive stiffness in auxetic magneto-mechanical metamaterials *Proc. R. Soc.* A **474** 20180003

[20] Almgren R F 1985 An isotropic three-dimensional structure with Poisson's ratio = −1 *J. Elast.* **15** 427–30

[21] Gibson L J and Ashby M F 1982 The mechanics cellular materials of two-dimensional cellular materials *Proc. R. Soc.* A **382** 43–59

[22] Kolpakov A G 1985 Determination of the average characteristics of elastic frameworks *J. Appl. Math. Mech.* **49** 739–45

[23] Wojciechowski K W 1987 Constant thermodynamic tension Monte Carlo studies of elastic properties of a two-dimensional system of hard cyclic hexamers *Mol. Phys.* **61** 1247–58

[24] Lakes R S 2017 Negative-Poisson's-ratio materials: auxetic solids *Annu. Rev. Mater. Res.* **47** 63–81

[25] Panico M, Langella C and Santulli C 2017 Development of a biomedical neckbrace through tailored auxetic shapes *Ital. J. Sci. Eng.* **1** 105–17

[26] Kapnisi M *et al* 2018 Auxetic cardiac patches with tunable mechanical and conductive properties toward treating myocardial infarction *Adv. Funct. Mater.* **28** 1800618

[27] Duncan O *et al* 2018 Review of auxetic materials for sports applications: expanding options in comfort and protection *Appl. Sci.* **8** 841

[28] Groeger D and Lasec S J 2019 pp 1–14

[29] Li Q, Kuang Y and Zhu M 2017 Auxetic piezoelectric energy harvesters for increased electric power output *AIP Adv.* **7** 015104

[30] Masters I G and Evans K E 1996 Models for the elastic deformation of honeycombs *Compos. Struct.* **35** 403–22

[31] Gibson L J and Ashby M F 1982 The mechanics cellular materials of three-dimensional cellular materials *Proc. R. Soc.* A **382** 43–59

[32] Alderson A, Alderson K L, Attard D, Evans K E, Gatt R, Grima J N, Miller W, Ravirala N, Smith C W and Zied K 2010 Elastic constants of 3, 4 and 6-connected chiral and anti-chiral honeycombs subject to uniaxial in-plane loading *Compos. Sci. Technol.* **70** 1042–8

[33] Grima J N, Gatt R and Farrugia P S 2008 On the properties of auxetic meta-tetrachiral structures *Phys. Status Solidi* b **245** 511–20

[34] Grima J N, Farrugia P S, Gatt R and Attard D 2008 On the auxetic properties of rotating rhombi and parallelograms: a preliminary investigation *Phys. Status Solidi* b **245** 521–9

[35] Grima J N, Zammit V, Gatt R, Alderson A and Evans K E 2007 Auxetic behaviour from rotating semi-rigid units *Phys. Status Solidi* b **244** 866–82

[36] Grima J N and Evans K E 2006 Auxetic behavior from rotating triangles *J. Mater. Sci.* **41** 3193–6

[37] Grima J N, Alderson A and Evans K E 2004 Negative Poisson's ratios from rotating rectangles *Comput. Methods Sci. Technol.* **10** 137–45

[38] Grima J N and Evans K E 2000 Auxetic behavior from rotating squares *J. Mater. Sci. Lett.* **19** 1563–5

[39] Slann A, White W, Scarpa F, Boba K and Farrow I 2015 Cellular plates with auxetic rectangular perforations *Phys. Status Solidi* b **252** 1533–9

[40] Strek T *et al* 2017 Computational modelling of structures with non-intuitive behaviour *Materials* **10** 1386

[41] Tang Y, Lin G, Han L, Qiu S, Yang S and Yin J 2015 Design of hierarchically cut hinges for highly stretchable and reconfigurable metamaterials with enhanced strength *Adv. Mater.* **27** 7181–90

[42] Wang G *et al* 2019 Large deformation shape optimization of cut-mediated soft mechanical metamaterials *Mater. Res. Express* **6** 055802

[43] Kolken H M A, Janbaz S, Leeflang S M A, Lietaert K, Weinans H H and Zadpoor A A 2018 Rationally designed meta-implants: a combination of auxetic and conventional meta-biomaterials *Mater. Horiz.* **5** 28–35

[44] Yang L, Harrysson O, West H and Cormier D 2012 Compressive properties of Ti-6Al-4V auxetic mesh structures made by electron beam melting *Acta Mater.* **60** 3370–9

[45] Warmuth F *et al* 2017 Fabrication and characterisation of a fully auxetic 3D lattice structure via selective electron beam melting *Smart Mater. Struct.* **26** 025013

[46] Mitschke H, Schwerdtfeger J, Schury F, Stingl M, Körner C, Singer R F, Robins V, Mecke K and Schröder-Turk G E 2011 Finding auxetic frameworks in periodic tessellations *Adv. Mater.* **23** 2669–74

[47] Sorrentino A, Castagnetti D, Spaggiari A and Dragoni E 2019 Shape optimization of the fillet under a bolt's head *J. Strain Anal. Eng. Des.* **54** 247–53

[48] Pedersen N L 2013 Overall bolt stress optimization *J. Strain Anal. Eng. Des.* **48** 155–65

[49] Rafi H K, Karthik N V, Gong H, Starr T L and Stucker B E 2013 Microstructures and mechanical properties of Ti6Al4V parts fabricated by selective laser melting and electron beam melting *J. Mater. Eng. Perform.* **22** 3872–83

[50] Spadoni A, Ruzzene M and Scarpa F 2006 Dynamic response of chiral truss-core assemblies *J. Intell. Mater. Syst. Struct.* **17** 941–52

[51] Wang Y C and Lakes R S 2005 Composites with inclusions of negative bulk modulus: extreme damping and negative poisson's ratio *J. Compos. Mater.* **39** 1645–57

[52] Smith M 2009 *ABAQUS/Standard User's Manual, Version 6.9* (United States: Dassault Systèmes Simulia Corp)

[53] Mizzi L *et al* 2020 Implementation of periodic boundary conditions for loading of mechanical metamaterials and other complex geometric microstructures using finite element analysis *Eng. Comput.* (https://doi.org/10.1007/s00366-019-00910-1)

[54] Poźniak A A, Wojciechowski K W, Grima J N and Mizzi L 2016 Planar auxeticity from elliptic inclusions *Composites* B **94** 379–88

[55] Omairey S L, Dunning P D and Sriramula S 2019 Development of an ABAQUS plugin tool for periodic RVE homogenisation *Eng. Comput.* **35** 567–77

[56] Vanderplaats research development VisualDOC 8.0 (available at: www.vrand.com/about-us/)

[57] Van Rossum G and Drake J F L 1995 *Python Reference Manual* (Amsterdam: Centrum voor Wiskunde en Informatica)

[58] Mirjalili S 2019 Particle swarm optimisation *Stud. Comput. Intell.* **780** 15–31

[59] Grima J N, Alderson A and Evans K E 2005 Auxetic behaviour from rotating rigid units *Phys. Status Solidi* b **242** 561–75

[60] Graphwork. Graphwork

[61] Mizzi L, Salvati E, Spaggiari A, Tan J-C and Korsunsky A M 2020 Highly stretchable two-dimensional auxetic metamaterial sheets fabricated via direct-laser cutting *Int. J. Mech. Sci.* **167** 105242

[62] Mizzi L and Spaggiari A 2020 Lightweight mechanical metamaterials designed using hierarchical truss elements *Smart Mater. Struct.* **29** 105036

[63] Attard D and Grima J N 2012 A three-dimensional rotating rigid units network exhibiting negative Poisson's ratios *Phys. Status Solidi* b **249** 1330–8

[64] Rueger Z, Ha C S and Lakes R S 2019 Flexible cube tilt lattice with anisotropic cosserat effects and negative Poisson's ratio *Phys. Status Solidi* b **256** 1–6

[65] Kim J *et al* 2017 Structures with polygonal prisms for three-dimensional auxetic behaviour *Proc. R. Soc.* A **473** 20160926